1 **Icy Saturnian Satellites: Disk-Integrated UV-IR Characteristics and Links to**

2 **Exogenic Processes**

3

4 Amanda R. Hendrix* (arh@psi.edu); 310-922-3414

5 Planetary Science Institute, 1700 East Fort Lowell, Suite 106, Tucson, AZ 85719

6

7 Gianrico Filacchione

8 INAF, Institute for Astrophysics and Planetary Sciences from Space, Rome, IT

9

10 Chris Paranicas

11 Applied Physics Laboratory, Johns Hopkins University, Laurel, MD

12

13 Paul Schenk

14 Lunar and Planetary Institute, Houston, TX

15

16 Roger Clark

17 Planetary Science Institute, Tucson, AZ

18

19 Francesca Scipioni

20 NASA Ames Research Center, Mountain View, CA

21

22 *corresponding author

23

29

30

31   **Highlights.**

32   • Combined Cassini data result in hemispheric composite spectra of Saturn's moons.

33   • Ultraviolet and visible spectral trends are compared with exogenic processes.

34   • Results are consistent with E ring organics being responsible for coloring the moons.

35   • Electrons in the tens of keV range may be particularly effective at darkening and

36   reddening.

37

38

Abstract.

Combined Cassini observations obtained at similar observing geometries in the ultraviolet through infrared spectral range, along with additional UV data from Hubble Space Telescope where available, are used to study system-wide trends in spectral albedos of the inner icy Saturnian satellites (Mimas, Enceladus, Tethys, Dione, Rhea). We compare derived UV and visible geometric albedos, and UV absorption strengths, of the leading and trailing hemispheres with E ring grain flux and charged particle intensities (electrons and ions of varying energies) to those hemispheres. We find that the UV absorption strength on the leading hemispheres is anti-correlated with E ring grain flux. On the trailing hemispheres, the UV absorption strength is correlated with intensity of electrons in the tens of keV range. We suggest that these relationships could imply links with the organic component of the E ring. Radiolytic processing of organics causes the products to become spectrally redder, increasing the UV absorption strength. Such processing occurs while organic-rich grains are in the E ring, and increases with exposure time in the E ring, such that grains interacting with Rhea are redder (more processed) than those impacting Tethys. Further processing occurs on the trailing hemispheres of the satellites, via radiolysis by electrons in the tens of keV range.

1. Introduction.

The inner moons of Saturn – Mimas, Enceladus, Tethys, Dione and Rhea - exhibit remarkable **large spatial scale** albedo and color variations. The albedo trends with orbital distance can be linked to a combination of processes including E-ring grain bombardment and charged particle bombardment, as discussed by Schenk et al. (2011). One of the fascinating concepts Cassini has learned about the Saturn system is that, though their surface compositions are dominated by water ice, and evidently linked to E ring grain bombardment (Buratti et al., 1990; Verbiscer et al., 2007), the icy satellites are spectrally red: they are absorbing in the ultraviolet-visible wavelength region (wavelengths <~550 nm) – a spectral characteristic not typical of water ice. This spectral behavior was revealed initially, using HST data, for the leading and trailing hemispheres of Rhea and Dione (Noll et al., 1997) and also shown in HST data for Enceladus and Tethys (hemispheres not specified) (Noll, 2008). Cassini instruments have confirmed this spectral behavior for all hemispheres of all of the inner medium sized moons of Saturn, including Mimas. Thus, some basic questions are: What is the species or process that causes this UV-visible spectral redness? Is the absorber a photolytic or radiolytic (i.e. space weathered) product, or a combination of both? Is it native to the Saturn system? What is the relationship (if any) to the Enceladus plume gases and E-ring? Here, we utilize a system-wide study of UV-visible color trends to aid in understanding the source of the absorber(s).

The oft-used approach to answering surface composition questions is to use visible and near-infrared (VNIR) spectra, and indeed this has been done with success in the Saturnian system (e.g., Clark *et al*., 2008; Verbiscer *et al*., 2006; Filacchione *et al*., 2010).

However, VNIR spectra alone often do not tell the entire compositional story. The reddish UV-visible absorption, present to varying degrees on all of the satellites, could be due to several contributors, all of which are not very spectrally active in the near-IR, so they cannot be uniquely identified by Cassini's Visible-Near Infrared Mapping Spectrometer (VIMS) alone. In this study, we investigate the system-wide trends affecting the surface compositions of Saturn's inner icy moons by creating composite spectra at UV-IR wavelengths (100-5000 nm) using data from Cassini Ultraviolet Imaging Spectrograph (UVIS), Imaging Science Subsystem (ISS) and Visual and Infrared Mapping Spectrometer (VIMS).

Whereas Verbiscer et al. (2007) relate global visible geometric albedos of the moons to the I/F of the E ring, here we look at visible and UV (300 nm) geometric albedos and UV absorption depths of the leading and trailing hemispheres, to understand their relationships to E ring flux, plasma flux and energetic electron intensity. Schenk et al. (2011) describe possible effects of dust, plasma and energetic electrons on the visible color; here we use composite spectra to quantify those effects, and focus on effects in the UV (albedo and absorption).

2. Background.

Previous Results.

Icy satellite data from Cassini VIMS, ISS and UVIS have been analyzed independently in the past, to produce useful results about the surface compositions and interactions with the environments of these bodies. Here we describe some of the results that have been obtained.

103   At visible wavelengths, a moderate negative (or blue) to neutral 350-550 nm slope

104   and high albedos are associated with fresh water icy surfaces. A moderate to positive (or

105   red) slope has been suggested to be the result of contamination induced by the presence

106   of very different materials, including complex organics produced by irradiation of simple

107   hydrocarbons (e.g. Moore et al., 1983; Moore and Hudson, 1998; Delitsky et al., 2017),

108   amorphous silicates (Poulet et al., 2003), carbonaceous particles (Cuzzi and Estrada,

109   1998), nanophase iron or hematite (Clark et al., 2008, 2012), tholins intimately mixed in

110   water ice grains (Ciarniello et al., 2011) or combinations of these materials.

111   Filacchione et al. (2010, 2012) performed a detailed studies of the entire suite of

112   VIMS disk-integrated observations of the icy satellites. For each satellite the disk-

113   integrated spectral slopes have been measured over two spectral ranges (350-550 and

114   550-950 nm). Some salient features arise in the groupings in the slope-slope plots over

115   these ranges. Mimas and Tethys have very flat slopes in the 550-950 nm range and

116   reddish slopes in the 350-550 nm range. Dione is also reddish in the 550-950 nm range

117   and distinctly bluer in the 550-950 nm range. Enceladus is also blue in the 550-950 nm

118   range and clearly also bluer than the other moons in the 350-550 nm range. Rhea is

119   redder than the other moons in both spectral ranges.

120   While the results of Filacchione et al. (2010, 2012) reveal the broad characteristics in

121   the 350-550 nm and 550-950 nm ranges and trace their radial distribution in the Saturnian

122   system (Filacchione et al., 2013), the results of Clark et al. (2008, 2012) and Stephan et al.

123   (2010, 2011) tell us about the finer-scale spectral features, mainly longward of 1000 nm.

124   The dominant VIMS-measured spectral features are due to H_2O ice. In addition to H_2O

125   ice, Clark et al. find evidence of trace amounts of CO_2, NH- and CH-bearing species and

126   H_2 on all the satellites. They also measure a variable blue peak, a local maximum in the

127   reflectance spectrum near 500 nm; shortward of this peak is the UV absorption. The blue

128   peak seems to be strongest in regions of intermediate abundances of dark material (e.g.,

129   at Dione) and at intermediate phase angles, but this needs to be studied further. Clark et al.

130   (2012) find that the best explanation for the blue peak, as well as the UV absorption, may

131   be sub-micron-sized H_2O ice in addition to nanograin hematite and nanograin iron; they

132   suggest that fine-grained metallic iron dust, e.g. in space-weathered meteorite dust,

133   contaminates the ice and that the competition of sub-micron ice, iron and hematite creates

134   the varying blue peaks and UV absorption observed throughout the system. **Rayleigh**

135   **scattering occurs when the size parameter x ($=2\pi D/\lambda$) <<1 (where D is the grain size**

136   **and λ is the wavelength); the blue peak is thought to be produced via Rayleigh**

137   **scattering by fine grains (e.g. Clark et al., 2008).**

138   The most significant analysis of ISS color data of Saturn's icy satellites so far has

139   been the work of Schenk et al. (2011), who constructed 3-color images using ISS

140   IR3/GRN/UV3 filters. They tracked color variations across the moons and linked large-

141   scale color patterns with exogenic processes. Some of the key results of Schenk *et al.*

142   include the mapping of blue-ish "lens" regions on the low latitude regions of the leading

143   hemispheres of Mimas and Tethys, the result of interactions with retrograde energetic **(~1**

144   **MeV)** electrons (Paranicas *et al.*, 2011). The relative blue-ness of the lens regions means

145   that they are relatively bright in the UV3 band range (centered at ~340 nm). The

146   interaction between the energetic electrons and the icy surfaces also results in regions of

147   relatively high thermal inertia (Howett et al., 2011). Spatial correlations are observed also

148   between equatorial lens regions and **daytime** temperatures inferred from reflectance

149   spectral behavior at 3600 nm (Filacchione et al., 2016).

150   Another key result of the Schenk et al. (2011) paper was the color map of Enceladus

151   plume fallout. The majority of the material from the plume is deposited on the surface in

152   the southern hemisphere with two wide fallout regions extending to the north between

153   180° and 270°W, and between 0° and 90°W (Kempf et al., 2010). This plume fallout

154   material is seen to be relatively blue-ish in the ISS images**; we suggest this is** due to an

155   increased abundance of fresh water ice. Notably, the regions not dominated by plume

156   fallout, which are likely dominated by E ring grains, are not bluish, they are yellow-ish.

157   The Cassini Ultraviolet Imaging Spectrograph (UVIS) covers the far-ultraviolet (far-

158   UV or FUV) spectral range, which includes a strong water ice absorption edge near 165

159   nm (Hendrix and Hansen, 2008). The water ice absorption edge dominates the UVIS

160   spectra of nearly every observed region on the icy satellites; however the slope of the

161   absorption edge can change, depending on the non-water ice species that are present, and

162   the magnitude and spectral shape of the spectrum longward and shortward of the 165 nm

163   edge can also vary depending on what other species are present.

164   Hendrix et al. (2010) pointed out, after careful photometric analyses of Enceladus

165   observations, that Enceladus has a lower-than-expected albedo in the 180-190 nm region.

166   (In fact, all of the icy moons are dark in the 180-190 nm range.) It was expected that

167   Enceladus' surface would be dominated by water ice, which has an albedo near unity in

168   this wavelength range; however, Enceladus' geometric albedo was closer to only ~0.3

169   (Hendrix et al., 2010). It was determined, by comparisons with broad-band data from

170   Hubble Space Telescope (HST), that to match Enceladus' spectral behavior a species that

171   absorbs rather steeply in the near-UV region (*i.e.,*between ~200 and 400 nm) must be

172   present. In that work, it was noted that NH_3 absorbs steeply in the near-UV, and is also

173   present in small amounts in the Enceladus plume (Waite *et al.,* 2009); a small amount of

174   NH_3 (<1%) is sufficient on the surface to replicate the absorption implied by the UVIS-

175   measured albedo. Hendrix et al. (2010) found that a species (more slowly absorbing than

176   NH_3) may also be present, such as a small amount of some type of tholin. More recent

177   HST data from the Cosmic Origins Spectrograph covering the 190-250 nm region are in

178   agreement with the UVIS data and the NH_3/tholin suggestion (Zastrow *et al.,* 2012).

179   Spectral modeling of VIS-IR Enceladus disk-integrated reflectance spectra by VIMS

180   indicates that an intraparticle mixture of 99.992% crystalline water ice and 0.008% Triton

181   tholin with grains of 63 μm is able to best fit the observations (Filacchione *et al.*, 2012).

182   Mimas is also very dark in the far-UV, but exhibits an interesting far-UV albedo

183   variation across the surface; the leading-southern region was measured (in February 2010,

184   a few months after equinox, when the sun began to move toward the north) to be darker

185   than other regions. The trailing hemisphere is the brightest region, likely due to

186   emplacement of relatively bright E-ring grains there. We have suggested (Hendrix et al.,

187   2012) that photolytically-produced hydrogen peroxide (H_2O_2) could be responsible for

188   the dark southern region. H_2O_2 is readily created in the uppermost layers of the icy

189   regolith that are sensed by UVIS, and absorbs strongly in the UV. The pathlengths sensed

190   by UVIS **(on the order of a few microns (Hendrix et al., 2012))** are generally not long

191   enough to detect the effects of the energetic electrons seen at longer wavelengths. At 340

192   nm **(where sensing depths are ~cm, (Hendrix et al., 2012)),** the energetic electron "lens"

193   is sensed by ISS (Schenk et al., 2011); the lens is relatively bright (blue) at 340 nm.

194 However, the production of H_2O_2 in the uppermost layers of the regolith may be enough

195 to largely mask the lens from UVIS. That being said, UVIS does likely sense a hint of the

196 lens in the "ansa" region – this is where the electron precipitation is more concentrated in

197 area (Hendrix et al., 2012) and where the lens is most prominent. The lens corresponds to

198 a thermal anomaly area where both CIRS (Howett et al., 2011) and VIMS (Filacchione et

199 al, 2016) have measured lower temperatures with respect to the nearby terrains. The best

200 fit to the disk-integrated Mimas reflectance measured by VIMS is achieved by means of

201 two populations of contaminants: 1) 0.1% tholin in intraparticle mixing with 97.9% water

202 ice grains and 2) 2% amorphous carbon in intimate mixing, with grain size of 58 μm

203 (Filacchione et al., 2012).

204

205 *Processes.*

206 In this study, we consider disk-integrated spectra of the moons, which we expect

207 are controlled more by exogenic processes than by endogenic/geologic processes that

208 would be expected to operate on smaller, more localized scales. Furthermore, in

209 considering the UV-visible spectral shape and albedos, we are mindful that these are

210 characteristics of the uppermost surface layer, so consider that they are related closely to

211 exogenic effects.

212 Bombardment by plasma and energetic electrons. Corotating cold plasma will tend to

213 impact the trailing hemispheres of the icy moons (centered on 270°W), often resulting in

214 a darkening of the surfaces in a target shape related to the cosine of the angle to the

215 plasma ram direction. Radiolysis by electrons and ions has important chemical effects as

216 well, producing species such as H_2O_2, O_2 and O_3 in the water ice-rich regoliths (e.g.

217 Johnson et al., 2008). **Most electrons preferentially hit the trailing hemisphere but**

218 **those greater than about 0.5 to 1.5 MeV preferentially hit the leading (Paranicas et**

219 **al., 2011; Nordheim et al., 2017); this interaction results** in an increase in thermal

220 inertia (Howett et al., 2011) and creating the blue lens-shaped feature (Schenk *et al.*,

221 2011).

222 <u>E-ring grain coating/bombardment.</u> Hamilton and Burns (1994) showed that E-ring

223 grains will tend to impact primarily the trailing hemisphere of Mimas and the leading

224 hemispheres of the satellites that orbit outside Enceladus' orbit (Tethys, Dione, Rhea).

225 Juhasz and Horanyi (2015) provide updated models of the dust interactions, wherein the

226 bombardment on Tethys **and Rhea is focused more toward the** sub- and anti-Saturnian

227 parts of the leading hemisphere **rather than toward the apex of the leading**

228 **hemisphere**. E-ring grain bombardment has been suggested to have a brightening effect

229 on the satellites, affecting the overall visible-wavelength brightness of all the inner

230 moons (Verbiscer *et al.,* 2007) due to coating of the surface with fresh material and/or

231 sandblasting of the grains **(Hamilton and Burns, 1994)**. We note that, despite these

232 effects of E-ring grain bombardment, however, *the surfaces of the satellites are UV dark*

233 (as seen by UVIS, discussed above) – implying that if E-ring grains dominate the optical

234 properties of the surfaces, then we are sensing in the UV-visible a non-ice component of

235 the E-ring (because H_2O ice is bright in the UV). Or those non-ice components could be

236 darkened/altered by weathering that occurs on the same timescale as E ring grain

237 bombardment (e.g., Hand and Carlson 2015 and references therein). Cassini's Cosmic

238 Dust Analyzer (CDA) indicates that E ring grains are made up of two primary types of

239 grains. Type-1 grains are pure water ice particles (Postberg et al., 2008). Type-2 grains,

240 comprising ~25% of E-ring grains, are dominated by organic species (Postberg *et al.*,

241 2008, 2017). Salts are observed by CDA in the plume grains but are depleted in the

242 population of grains escaping to the E ring (Postberg et al., 2009). Silicate dust streams

243 have also been observed using CDA (Hsu et al., 2011).

244   Photolysis. Photolysis is a very efficient process for breaking up water ice (in the

245 uppermost few microns of the regoliths) and producing species such as H_2O_2. Photolysis

246 could play a role in the production of O_3 at Rhea and Dione (Noll et al., 1997), and is key

247 in the production of Saturn's rings' O_2 atmosphere (Johnson et al., 2006). As mentioned,

248 Hendrix et al. (2012) suggest that photolytically-produced H_2O_2 is present in the topmost

249 layer of Mimas' regolith, as detected by UVIS.

250   Bombardment by exogenic dark material. **Clark et al. (2008, 2012) suggested, based**

251 **on high resolution imaging and spectroscopy, that there is an exogenic source of**

252 **dark material, onto the trailing hemispheres of Dione (Clark et al., 2008; Stephan et**

253 **al., 2010) and Rhea (Stephan et al., 2012), where it is observed that the older**

254 **terrains have higher concentrations of dark materials.** The exogenic source is unclear;

255 the Phoebe ring (Verbiscer et al., 2009) is a possible source, though its retrograde-

256 orbiting grains would impact mainly the leading hemisphere of Dione, and are considered

257 of very low flux inside of Titan's orbit (Tamayo et al., 2011). Another source is

258 meteoritic dust which Cuzzi et al. (2009 and references therein) have argued is a source

259 of contamination of the main rings. The dark material (Stephan et al., 2010; 2012) could

260 be linked to an exogenic process such as magnetospheric processing and on smaller

261 scales the dark material is interrupted by craters and/or geologic terrains (e.g. graben).

262

3. Instruments and Datasets.

To investigate the problem of the UV-visible absorber in the Saturnian system, we create composite disk-integrated spectra of of Mimas, Enceladus, Tethys, Dione and Rhea, using data from Cassini VIMS, ISS and UVIS. **Because many of the exogenic processes discussed in Sec. 2 may result in leading-trailing hemispheric differences, we analyzed disk-integrated spectra of both the leading and trailing hemispheres of Tethys, Dione and Rhea. In the case of Mimas, disk-integrated observations are limited and we were unable to find satisfactory observations of both the leading and trailing hemispheres. For Enceladus, because previous observations had indicated that leading-trailing asymmetries are largely insignificant, we opted to include just a single observation in our analysis.**

The VIMS instrument (Brown et al., 2004) covers the 0.35-5.1 μm spectral range by imaging a 1.8° FOV with 64 pixels. The experiment consists of two imaging spectrometers (VIS and IR) observing the same field of view in two spectral ranges. VIMS-V is the Italian-made imaging spectrometer covering the 0.35–1.05 μm range in 96 spectral channels and spatial resolutions of 500 x 500 (nominal) or 166 x 166 (high resolution) μrad/pixel (Miller *et al.,* 1996). VIMS-IR is the US-made channel covering the 0.8-5.1 μm spectral range with 256 spectral channels and spatial resolutions of 500 (nominal) or 500 x 250 (high resolution) μrad/pixel.

The Cassini imaging science sub-system (ISS) consists of two cameras, the narrow angle camera (NAC) and the wide angle camera (WAC) (Porco et al., 2004). Both cameras use a 1024 x 1024-element charge-coupled device (CCD) array detector. Image scale is 5.9907 μrad/pixel for the NAC and 59.749 μrad/pixel for the WAC. In-flight

286   calibration of the cameras is described by West et al. (2010). Each camera contains two

287   filter wheels; the filter coverage for the NAC is shown in Porco et al. (2004). For the

288   purposes of this study, we have focused on observations where ISS has used one or more

289   of its UV filters, UV1 (258 nm), UV2 (298 nm) or UV3 (338 nm), to extend spectral

290   coverage as close to UVIS as possible.

291   The UVIS (Esposito et al., 2004) far-UV channel covers the ~100-194 nm region.

292   UVIS provides simultaneous spectral and one-dimensional spatial images. The detector

293   format is 1024 spectral pixels by 64 spatial pixels. Each spatial pixel subtends an angle of

294   1 mrad projected on the sky. The low-resolution slit has a spectral resolution of 0.48 nm

295   and subtends an angle of 1.5 mrad. The high-resolution slit has a spectral resolution of

296   0.275 nm and subtends an angle of 0.75 mrad; this slit is usually used for close-up

297   satellite encounters. The second spatial dimension is acquired by slewing the UVIS slit

298   across the target body.

299   Due to the synergistic nature of the Cassini spacecraft and the Icy Satellites Planning

300   Group, during most icy satellites observations, all remote sensing instruments participate,

301   so that simultaneous ISS, UVIS and VIMS data are acquired. UVIS, ISS and VIMS are

302   all boresighted, so simultaneous **disk-integrated** observations of the same target are

303   straightforward. To create disk-integrated composite spectra of the icy satellites, we use

304   simultaneous observations where possible. This eliminates the need to photometrically

305   correct one dataset to match another. This is challenging however, due to resolution

306   issues: the distant observations that are most useful for UVIS (when the target body is

307   <1.5 mrad across, it fits entirely within the UVIS slit) tend to be too low in resolution for

308   VIMS. So we have in several cases found it useful to use non-simultaneous observations

309   of similar geometry (i.e. similar phase angle and sub-spacecraft longitude). **For non-**

310   **simultaneous observations, we have used observations at as-similar-as-possible**

311   **phase angles; we estimate (based on phase curves from Royer and Hendrix (2014)**

312   **that the phase angle differences are small enough (e.g. between ISS and UVIS) that**

313   **we are not introducing a significant spectral shift in our composite spectra.** Using

314   observations of identical viewing geometry, we have confirmed good agreement between

315   ISS and VIMS at overlapping wavelengths, so we can overplot non-simultaneous VIMS

316   data (of the appropriate hemisphere) for some observations by scaling to ISS. VIMS and

317   ISS data have a region of spectral overlap; there is a small gap between UVIS and ISS

318   (194-~260 nm) but we nevertheless obtain a strong sense of the shape of the spectrum in

319   the region. In this report, we use HST Space Telescope Imaging Spectrometer (STIS) and

320   Faint Object Spectrograph (FOS) data to fill in the spectral gap between ISS and UVIS,

321   where HST data are available. Knowing the ISS-measured whole-disk albedo for a

322   particular observational geometry, we can simply overplot the existing HST data using

323   the overlap in wavelength coverage, increasing the spectral coverage.

324

325   **4. Results: Composite Spectra**

326   Disk-integrated spectra of the icy moons, using combined data from Cassini and from

327   HST instruments, are shown in Fig. 1. Information on the observations that were used for

328   these composite spectra is shown in Table 1. These composite spectra (Fig. 1) highlight

329   regional compositional variations within the inner Saturnian system. The spectra of all

330   these satellites are bright and spectrally relatively flat at visible wavelengths longer than

331   ~500 nm; the water ice absorption features near 1.5, 2.0 and 3.0 μm dominate the infrared

332   spectrum. Shortward of 500 nm the surfaces become absorbing with decreasing

333   wavelength, resulting in reddish spectra. The satellites exhibit flattish-to-bowl-shaped

334   spectra in the ~200-350 nm range and demonstrate the 165 nm water ice absorption edge,

335   in varying strengths. The HST spectra demonstrate the broad band at 260 nm discussed

336   by Noll et al. (1997) (here we do not focus on the cause of the absorption and rather focus

337   on the UV dropoff). On Dione and Rhea, the composite spectra may require a dramatic

338   decrease in reflectance near 200 nm, in order to meet up with the UVIS data (but the

339   HST/FOS data for Dione and Rhea do not have the spectral extent of the STIS data

340   shown for Enceladus and Tethys).

341   In Fig. 2, we show normalized spectra of the leading and trailing hemispheres of

342   Tethys, Dione and Rhea to directly compare these regions. These plots show that the UV-

343   visible absorber is stronger on the trailing hemisphere of Tethys and Dione than on those

344   leading hemispheres, and that the leading-trailing spectral dichotomy is strongest on

345   Tethys and minimal on Rhea. The differences in water ice absorption band depths in the

346   IR (near 1.5 and 2 microns) have largely been attributed to grain size differences (e.g.

347   Stephan *et al.* 2010; Scipioni et al., 2013, 2014). The comparison between the disk-

348   integrated UV-visible (100-900 nm) spectrum of Rhea's leading and trailing hemispheres

349   shows no significant spectral differences. However, since we know that Rhea's LH is

350   brighter than its trailing hemisphere (e.g. Verbiscer et al., 2007; see also Table 2), this

351   suggests that (a component of) Rhea's trailing hemisphere darkening agent is spectrally

352   bland throughout the ~150-900 nm region. The IR water ice absorption depths on Rhea's

353   leading and trailing hemispheres are similar in depth, consistent with overall similar

354   water ice grain sizes and abundances.

355   Figure 3 displays all normalized reflectance spectra together. The UV absorption edge

356   that begins at ~500 nm is strongest for Rhea, the trailing hemispheres of Dione and

357   Tethys, and possibly Mimas; it is least strong for Enceladus and the leading hemispheres

358   of Dione and Tethys. This UV absorption edge strength translates to lower albedos in the

359   far- and near-UV for Rhea and the trailing hemispheres of Dione and Tethys, and higher

360   far- and near-UV albedos for Mimas and the leading hemispheres of Dione and Tethys;

361   Enceladus exhibits the highest far- and near-UV albedo. This suggests that the absorbing

362   species is/are present in greater abundances on the trailing hemispheres of Dione and

363   Tethys and on Rhea. Absolute reflectance spectra are presented in Fig. 4, where we have

364   scaled by the visible albedos as listed in Table 2.

365

366   **5. Relationships with Exogenic Processes**

367   The composite spectra in Figs. 1-4 can be used to study the inner system surface

368   compositions of the satellites to understand large-scale exogenic effects. In Figs. 5 and 6

369   we compare the visible and UV geometric albedos and UV absorption depths (UV/visible

370   ratio) with E ring grain fluxes and electron fluxes to look for trends. In these figures, we

371   have used the 300 nm albedos from Fig. 4 as the UV albedo and to represent the UV

372   absorption, we use the ratio of the 300 nm albedo to the ~600 nm albedo from Fig. 4.

373   In Figure 5, E ring fluxes to the leading and trailing hemispheres have been estimated

374   based on the relative fluxes from Juhasz and Horanyi (2015) and Kempf et al. (2017,

375   their Fig. 11) (M. Horanyi, *pers. comm.*). The albedos of the leading hemispheres

376   decrease with E ring grain flux (Fig. 5a). On the trailing hemispheres (Fig. 5b), Mimas's

377   albedo is lower than expected if only related to E ring grain flux. (Verbiscer et al. (2007)

378　tied the overall (not leading or trailing hemisphere) visible albedo with E ring albedo, not

379　flux). The UV absorption (Figs. 5c and 5d) <u>increases</u> in strength with <u>decreasing</u> E ring

380　grain flux. The absorption is generally stronger on each trailing hemisphere, than on the

381　leading hemispheres.

382　　In Fig. 6, we compare albedo and UV absorption with intensity of tens of keV

383　electrons (using data from Paranicas et al., 2011). These electrons are expected to

384　primarily bombard the trailing hemispheres of the satellites (e.g. Patterson et al., 2012).

385　We find that the trailing hemisphere UV and visible albedos roughly decrease as electron

386　intensity increases (Fig. 6a). The UV absorption on the trailing hemisphere (Fig. 6b)

387　roughly increases with 35 keV electron intensity. The trailing hemisphere UV absorption

388　is similar for Tethys, Dione and Rhea, which may suggest some level of saturation. We

389　have also compared our leading and trailing hemisphere albedos and UV absorptions with

390　intensities of hundreds of keV to MeV electrons (Paranicas et al., 2011; Kollmann et al.,

391　2011), and with plasma electrons and ions (Persoon et al., 2006, 2009); we find that the E

392　ring grain and ~tens of keV electrons are the only species that appear to demonstrate

393　relationships with our leading hemisphere (E ring grain) and trailing hemisphere (tens of

394　keV electron) data. MeV particles could also cause the same absorbing effect but they are

395　so few in number that it is harder to see a correlation.

396　　In Fig. 6, the trailing hemisphere UV and visible albedos roughly decrease as electron

397　intensity (tens of keV) increases. The UV absorption on the trailing hemisphere increases

398　with 35 keV electron intensity; the UV absorption is similar for Tethys, Dione and Rhea,

399　suggesting some level of saturation. These plots use 35 keV electron intensity (Paranicas

400   et al., 2011) as a proxy for ~tens of keV electrons, which primarily impact the trailing

401   hemispheres.

402

403   **6. Discussion and Implications**

404   The relationships between observed UV absorption strength on the satellites and E

405   ring grain flux and electron intensity (Figs. 5 and 6) demonstrate correlations that, while

406   not implying causation, lead to potential implications for system-wide processing. We

407   suggest that the non-ice component of the E ring grains, namely the organic species,

408   plays an important role in coloring the surface of the satellites. Postberg et al. (2008,

409   2017) show that ~25% of E ring grains include an organic component. The evolution of

410   frozen hydrocarbons (e.g. CH_4) in the laboratory has been discussed (e.g. Strazzulla et al.,

411   1983a, 1983b; deVries et al., 1984; Foti et al., 1984; Strazzulla, 1986; Lanzerotti et al.,

412   1987; Compagnini et al., 2009); after dosing with protons, the hydrocarbons are

413   converted to a yellow organic residue. Upon further irradiation, the yellow organic

414   residue becomes brown and then black as carbonization occurs. We suggest that a similar

415   processing of grains occurs within the E ring, and that further processing occurs after the

416   E ring grains have impacted the surfaces of the satellites. Postberg et al. (2008) point out

417   that E ring grains have experienced plasma sputtering for several decades whilst reaching

418   the outer E ring near Rhea. **The timescales involved in the chemical processing**

419   **resulting in reddening are unclear; Brunetto et al. (2006) provide estimates for**

420   **reddening (in the 0.68-1.25 μm range, so longward of what we consider here) for 10**

421   **eV/16 amu, 50 eV/16 amu and 100 eV/16 amu cases. All cases provide significant**

422   **reddening (2-26%/1000 Å), though similar studies for the spectral region we**

423   **consider here were not found in a literature search. However, based on these results,**

424   **it is reasonable to assume that** the E ring grains that make it to Rhea are likely to be

425   redder and darker than the "fresher" ones that impact Tethys. Radiolysis by ~10 keV

426   electrons on the trailing hemispheres of the moons then further darken and redden the

427   material there. The region of higher E ring grain fluxes (close to Enceladus) is where E

428   ring grains are fresher and less processed due to lower electron (tens of keV) irradiation.

429   We see that satellites with lower E ring fluxes, and higher electron intensity (e.g. Rhea)

430   have strong UV absorption and lower albedos than satellites (e.g. Enceladus) with high E

431   ring grain fluxes and lower electron intensity. Our results show that electrons in the ~tens

432   of keV energy range may be particularly effective at reddening; this is consistent with

433   results (Hand and Carlson, 2015) in the Jovian system.

434   There is evidence in the Saturnian system for low-level carbonization occurring. In

435   Fig. 2, comparison between the disk-integrated UV-visible (100-900 nm) spectrum of

436   Rhea's leading and trailing hemispheres shows no significant spectral differences.

437   However, since we know that Rhea's leading hemisphere is brighter than its trailing

438   hemisphere (e.g. Verbiscer et al., 2007; see also Table 2), this suggests that (a component

439   of) Rhea's trailing hemisphere darkening agent is spectrally bland throughout the ~150-

440   900 nm region. This spectrally bland, low-albedo component could be E ring organics

441   that have been carbonized due to higher levels of processing (i.e. greater levels of

442   exposure).

443   These results of UV absorption strength in the Saturn system are consistent with those

444   of Filacchione et al. (2013), who used *Cassini* VIMS data to show that the spectral slope

445   (0.35-0.55 μm) increases (becomes redder) with distance from Enceladus. Filacchione et

446   al. (2013) noted that because Enceladus is the primary source of the E ring, that the E

447   ring grains likely play a role in influencing the spectral properties of the moons. Here we

448   present a related hypothesis, that the source of reddening is the organic component of the

449   E ring. We note that Clark et al. (2008, 2012) have shown that models including nano-

450   iron/nano-hematite can be used to fit VIMS spectra of Phoebe, Iapetus, Hyperion and

451   Dione, including the UV absorption and other spectral details. Here we suggest an

452   alternative model that is consistent with the composition of the E ring (~25% organics),

453   lab work on radiolysis of organic species, and observed large-scale trends in the inner

454   Saturnian system.

455

456   **7. Conclusions.**

457   We have compiled composite spectra of the Saturnian satellites using a combination

458   of Cassini UVIS, ISS and VIMS data, along with HST data. We have used these

459   composite spectra to investigate large-scale trends in the system relating to albedo and

460   UV absorption (i.e. reddening).

461   Our results show that both albedo and UV absorption are correlated with E ring grain

462   flux and electron intensity. On the leading hemispheres, the albedo increases with E ring

463   grain flux. On both the leading and trailing hemispheres, the UV absorption decreases in

464   strength with increasing E ring grain flux. On the trailing hemispheres, where electron

465   bombardment (in the tens of keV range) occurs, the albedo decreases, and the UV

466   absorption strength increases, with electron intensity. The UV absorption is also stronger

467   on the trailing hemispheres than on the leading hemispheres. We suggest that these trends

468   are related to the organic component of the E ring (~30% of the E ring grains). These

469   organics are expected to darken and redden with exposure, such that the grains impacting

470   Rhea are likely to be darker and redder (though fewer in number) than those that impact

471   Enceladus. In addition, the UV absorption, stronger on the trailing hemispheres than on

472   the leading hemispheres, is increased there due to continued radiolysis of the organics on

473   the surfaces of the moons. At Rhea, and likely at Dione as well, we suggest that some of

474   the dark component could be due to carbonization as a result of relatively high levels of

475   processing of those grains, both within the E ring and on the surfaces. Future studies of

476   the composite spectra, and spectral modeling of the UV-5 micron signatures, may help to

477   elucidate the exact nature of organic species.

478

484

485

486   **References.**

487   Brown, R.H., and 21 colleagues, 2004. The Cassini Visual and Infrared Mapping

488   Spectrometer (VIMS) investigation. Space Sci. Rev. 115, 111–168.

489   Buratti, B. J., Mosher, J. A., T. V. Johnson 1990. Albedo and color maps of the Saturnian

490   satellites. Icarus 87, 339-357.

491   Cassidy, T. Paranicas, C. P., Shirley, J. H., Dalton, J. B., III, Teolis, B. D., Johnson, R. E.,

492   Kamp, L., Hendrix, A. R. 2013. Magnetospheric ion sputtering and water ice grain

493   size at Europa. Planet. Space Sci. 77, 64-73.

494   Ciarniello, M. et al. 2011. Hapke modeling of Rhea surface properties through Cassini-

495   VIMS spectra. Icarus 214, 541-555.

496   Clark, R. N., Curchin, J. M., Jaumann, R., Cruikshank, D. P., Brown, R. H., Hoefen, T.

497   M., Stephan, K., Moore, J. M., Buratti, B. J., Baines, K. H., Nicholson, P. D., Nelson,

498   R. M. 2008. Compositional mapping of Saturn's satellite Dione with Cassini VIMS

499   and implications of dark material in the Saturn system. Icarus 193, 372-386.

500   Clark, R. N. D. P. Cruikshank, R. Jaumann, R. H. Brown, K. Stephan, C. M. Dalle Ore, K.

501   E. Livo, N. Pearson, J. M. Curchin, T. M. Hoefen, B. J. Buratti, G. Filacchione, K. H.

502   Baines, P. D. Nicholson 2012. The Surface Composition of Iapetus: Mapping Results

503   from Cassini VIMS. Icarus 218, 831-860.

504   Compagnini, G. L. D'Urso, O. Puglisi, G.A. Baratta, G. Strazzulla 2009. The irradiation

505   of solid hydrocarbons and the formation of linear carbon chains. Carbon 47, 1605-

506   1612.

507   Cuzzi, J. N. and P. R. Estrada 1998. Compositional Evolution of Saturn's Rings Due to

508   Meteoroid Bombardment. Icarus 132, 1-25.

509   Cuzzi, J.; Clark, R.; Filacchione, G.; French, R.; Johnson, R.; Marouf, E.; Spilker, L.

510   (2009) Ring Particle Composition and Size Distribution; in Saturn from Cassini-

511   Huygens. Edited by M.K. Dougherty, L.W. Esposito, and S.M. Krimigis. Berlin:

512   Springer, 2009. p.459-509

513   Delitsky, M. L., D. A. Paige, M. A. Siegler, E. R. Harju, D. Schriver, R. E. Johnson, P.

514   Travnicek 2017. Ices on Mercury: Chemistry of volatiles in permanently cold areas of

515   Mercury's north polar region. Icarus 281, 19-31.

516   deVries, A. E., R. Pedrys, R. A. Haring, A. Haring, F. W. Saris 1984. Emission of large

517   hydrocarbons from frozen CH_4 by keV proton irradiation. Nature 311, 39-40.

518   Esposito, L.W., and 18 colleagues, 2004. The Cassini Ultraviolet Imaging Spectrograph

519   investigation. Space Sci. Rev. 115, 299–361.

520   Filacchione, G., F. Capaccioni, R. N. Clark, J. N. Cuzzi, D. P. Cruikshank, A. Coradini, P.

521   Cerroni, P. D. Nicholson, T. B. McCord, R. H. Brown, B. J. Buratti, F. Tosi, R. M.

522   Nelson, R. Jaumann, and K. Stephan 2010. Saturn's icy satellites investigated by

523   Cassini-VIMS. II. Results at the end of nominal mission. Icarus 206, 507-523.

524   Filacchione, G. and 18 co-authors 2012. Saturn's icy satellites and rings investigated by

525   Cassini-VIMS. III. Radial compositional variability. Icarus 220, 1064-1096.

526   Filacchione, G., and 13 coauthors, 2013. The Radial Distribution of Water Ice and

527   Chromophores across Saturn's System. Astrophys. J. 766, Issue 2, article id. 76, 5 pp,

528   Filacchione, G. and 15 coauthors, 2016. Saturn's icy satellites investigated by Cassini

529   VIMS. IV. Daytime temperature maps. Icarus 271, 292-313.

530   Foti, G., Calcagno, L., K. L. Sheng, G. Strazzulla 1984. Micrometre-sized polymeter

531   layers synthesized by MeV ions impinging on frozen methane. Nature 310, 126-128.

532   Hamilton, D. P. and J. A. Burns, Origin of Saturn's E ring: Self-sustained, naturally,

533   Science, 264, 550-553, doi: 10.1126/science.264.5158.550, 1994.

534   Hand, K. P. and R. W. Carlson 2015. Europa's surface color suggests an ocean rich with

535   sodium chloride. Geophys. Res. Lett., 42, doi:10.1002/ 2015GL063559.

536   Hendrix, A.R., Hansen, C.J., 2008. Ultraviolet observations of Phoebe from the Cassini

537   UVIS. Icarus 193**,** 323–333.

538   Hendrix, A. R., C. J. Hansen, G. M. Holsclaw 2010. The Ultraviolet Reflectance of

539   Enceladus: Implications for Surface Composition. Icarus 206, 608-617.

540   Hendrix, A. R. Timothy A. Cassidy, Bonnie J. Buratti, Chris Paranicas, Candice J.

541   Hansen, Ben Teolis, Elias Roussos, E. Todd Bradley, Peter Kollmann, Robert E.

542   Johnson. 2012. The Albedo Pattern of Mimas at Far-Ultraviolet Wavelengths. Icarus

543   220, 922-931.

544   Howett, C. *et al.,* 2011 A high-amplitude thermal inertia anomaly of probable

545   magnetospheric origin on Saturn's moon Mimas. Icarus 216, 221-226.

546   Hsu H.-W., Postberg, F., Kempf, S., Trieloff, M., Burton, M., Roy, M., Moragas-

547   Klostermeyer, G., Srama, R. 2011 Stream particles as the probe of the dust-plasma-

548   magnetosphere interaction at Saturn. J. Geophys. Res. 116, Issue A9, CiteID A09215

549   Johnson, R. E. *et al.* 2006. Production, ionization and redistribution of O2 in Saturn's

550   ring atmosphere. Icarus 180, 292-402.

551   Johnson, R. E. *et al.* 2008. Sputtering of ice grains and icy satellites in Saturn's inner

552   magnetosphere. Planet Space Sci. 56, 1238-1243.

553   Juhász, A. and M. Horányi. Dust delivery from Enceladus to the moons of Saturn.

554   American Geophysical Union, Abstract 77479, 2015.

555   Kempf, S. et al., 2010. How the Enceladus dust plume feeds Saturn's E ring. Icarus 206,

556   446-457.

557   Kempf, S., M Horanyi, H.-W. Hsu, T. W. Hill, A. Juhasz, H. T. Smith 2017 Saturn's

558   Diffuse E Ring and its Connection With Enceladus in *Enceladus and the Icy Moons*

559   *of Saturn*, P. M. Schenk, R. N. Clark, C. J. A. Howett, A. J. Verbiscer, and J. H,

560   Waite, eds, U. Arizona Press, in review.

561   Kollmann, P., E. Roussos, C. Paranicas, N. Krupp, C. M. Jackman, E. Kirsch, K.-H.

562   Glassmeier 2011. Energetic particle phase space densities at Saturn: Cassini

563   observations and interpretations. J. Geophys. Res., 116, A05222,

564   doi:10.1029/2010JA016221.

565   Lanzerotti, L. J., W. L. Brown, K. J. Marcantonio 1987. Experimental study of erosion of

566   methane ice by energetic ions and some considerations for astrophysics. Astrophys. J.

567   313, 910-919.

568   Moore, M. H. and R. L. Hudson 1998. Infrared study of ion-irradiation water-ice

569   mixtures with hydrocarbons relevant to comets. Icarus 13, 518-527.

570   Moore, M. H., B. Donn, R. Khanna, M. F. A'Hearn 1983. Studies of proton-irradiated

571   cometary-type ice mixtures. Icarus 54, 388-405.

572   Noll, K. S. 2008. Ultraviolet spectra of icy satellites. Science of Solar System Ices,

573   abstract #9085.

574   Noll, K.S., Rousch, T.L., Cruikshank, D.P., Johnson, R.E., Pendleton, Y.J., 1997.

575   Detection of ozone on Saturn's satellites Rhea and Dione. Nature 388, 45–47.

576   **Nordheim, T. A., K. P. Hand, C. Paranicas, C. J. A. Howett, A. R. Hendrix, G. H.**

577   **Jones, A. J. Coates 2017. The near-surface electron radiation environment of**

578   **Saturn's moon Mimas. Icarus 286, 56-68.**

579   Paranicas, C., E. Roussos, N. Krupp, P. Kollmann, A.R. Hendrix, T. Cassidy, R.E.

580   Johnson, P. Schenk, G. Jones, J. Carbary, D.G. Mitchell, K. Dialynas 2011.

581   Energetic charged particle weathering of Saturn's inner satellites. Planet. Space Sci.

582   61, 60-65.

583   Patterson, G. W., C. Paranicas, L. M. Prockter 2012. Characterizing electron

584   bombardment of Europa's surface by location and depth. Icarus 220, 286-290.

585   Persoon, A. M., D. A. Gurnett, W. S. Kurth, J. B. Groene 2006. A simple scale height

586   model of the electron density in Saturn's plasma disk. Geophys. Res. Lett. 33,

587   L18106, doi:10.1029/2006GL027090.

588   Persoon, A. M. et al. 2009. A diffusive equilibrium model for the plasma density in

589   Saturn's magnetosphere. J. Geophys. Res. 114, A04211, doi:10.1029/2008JA013912

590   Porco, C. C. and 19 co-authors 2004. Cassini imaging science: instrument characteristics

591   and anticipated scientific investigations at Saturn. *Space Sci. Rev.* **115:** 363–497.

592   Postberg, F., Kempf, S., Hillier, J. K., Srama, R., Green, S. F., McBride, N., Grün, E.,

593   2008. The E-ring in the vicinity of Enceladus II. Probing the moon's interior—The

594   composition of E-ring particles. Icarus 193, 438-454.

595   Postberg, F., Kempf, S., Schmidt, J., Brillantov, N., Beinsen, A., Abel, B., Buck, U.,

596   Srama, R. (2009) Sodium salts in E ring ice grains from an ocean below the surface of

597   Enceladus. Nature 459, 1098–1101.

598   Postberg, F., N. Khawaja, S. Kempf, J.H. Waite, C. Glein, H.W. Hsu, R. Srama 2017.

599   Complex organic macromolecular compounds in ice grains from Enceladus. LPSC

600   XLVIII abstract #1401.

601   Poulet, F. D. P. Cruikshank, J. N. Cuzzi, T. L. Roush, R. G. French 2003 Compositions

602   of Saturn's rings A, B, and C from high resolution near-infrared spectroscopic

603   observations. Astron. Astrophys. 412, 305-316.

604   **Royer, E. M. and A. R. Hendrix 2014. First far-ultraviolet disk-integrated phase**

605   **curve analysis of Mimas, Tethys and Dione from the Cassini-UVIS data sets.**

606   **Icarus 242, 158-171.**

607   Schenk, P., D. Hamilton, R. Johnson, W. McKinnon, C. Paranicas, J. Schmidt, M.

608   Showalter 2011. Plasma, plumes and rings: Saturn system dynamics as recorded in

609   global color patterns on its midsize icy satellites. Icarus 211, 740-757.

610   Scipioni, F., Tosi, F., Stephan, K., Filacchione, G., Ciarniello, M., Capaccioni, F.,

611   Cerroni, P., and the VIMS Team, 2013. Spectroscopic classification of icy satellites

612   of Saturn I: Identification of terrain units on Dione. Icarus 226, 1331-1349.

613   Scipioni, F., Tosi, F., Stephan, K., Filacchione, G., Ciarniello, M., Capaccioni, F.,

614   Cerroni, P., and the VIMS Team, 2014. Spectroscopic classification of icy satellites

615   of Saturn II: Identification of terrain units on Rhea. Icarus 243, 1-16.

616   Stephan, K. and 14 co-authors 2010. Dione's spectral and geological properties. Icarus

617   206**,** 631-652.

618   Stephan, K. and 18 co-authors 2011. The Saturnian satellite Rhea as seen by Cassini

619   VIMS. Planet. Space Sci. 61, 142-160.

620   Strazzulla, G. 1986. Organic material from Phoebe to Iapetus. Icarus 66, 397-400.

621   Strazzulla, G., V. Pirronello, G Foti 1983a. Physical and chemical effects induced by

622   energetic ions on comets. Astron. Astrophys. 123, 93-97.

623   Strazzulla, G., L. Calcagno, G. Foti 1983b. Polymerization induced on interstellar grains

624   by low energy cosmic rays. Mon. Not. R. astr. Soc. 204, 59p-62p.

625   Tamayo D. et al 2011. Finding the trigger to Iapetus' odd global albedo pattern:

626   Dynamics of dust from Saturn's irregular satellites, Icarus 215.

627   Verbiscer, A. J., Peterson, D. E., Skrutskie, M. F., Cushing, M., Helfenstein, P., Nelson,

628   M. J., Smith, J. D., Wilson, J. C. 2006. Near-infrared spectra of the leading and

629   trailing hemispheres of Enceladus. Icarus 182, 211-223.

630   Verbiscer, A., French, R., Showalter, M., Helfenstein, P., 2007. Enceladus: Cosmic

631   graffiti artist caught in the act. Science 315, 815.

632   Verbiscer, A. J., M. F. Skrutskie, D. P. Hamilton 2009. Saturn's largest ring. Nature 461,

633   1098-1100.

634   Waite Jr., J.H., and 15 colleagues, 2009. Liquid water on Enceladus from observations of

635   ammonia and 40Ar in the plume. Nature 460, 487–490.

636   West, R. A. and 12 co-authors 2010. In-flight calibration of the Cassini imaging science

637   sub-system cameras. Planet. Space Sci. 58, 1475-1488.

638   Zastrow, M., J. T. Clarke, A. R. Hendrix, K. S. Noll. UV spectrum of Enceladus. Icarus

639   220, 29-35.

640

641

642

Table 1. Observation Geometry

Satellite		date	altitude	phase angle	sub-Cassini longitude
Mimas	UVIS	2005-265	778,733 km	43°	237°W
	ISS	2006-324	153,472 km	43°	223°W
	VIMS	2005-214	62,949 km	53°	232°W
Enceladus	UVIS	2008-178	1,283,650 km	15°	76°W
	ISS	2008-178	1,283,650 km	15°	76°W
	VIMS	2010-355	37,546 km	15°	163°W
Tethys	UVIS	2008-235	1,342,906 km	10°	59°W
	ISS	2008-235	1,342,906 km	10°	59°W
	VIMS	2008-294	1,154,802 km	8.6°	89°W
	UVIS	2005-264	1,377,469 km	59°	239°W
	ISS	2006-056	~145,000 km	63°	252°W
	VIMS	2004-302	3,948,311 km	65°	254°W
Dione	UVIS	2005-264	1,341,140 km	34°	95°W
	ISS	2011-275	203,530 km	26°	110°W
	VIMS	2005-284	~280,000 km	22°	120°W
	UVIS	2005-066	1,588,567 km	46°	311°W
	ISS	2005-214	242,838 km	44°	274°W
	VIMS	2005-213	~268,000 km	41°	257°W
Rhea	UVIS	2006-054	933,841 km	26°	92°W
	ISS	2006-055	356,446	27°	107°W
	VIMS	2008-232	429,608 km	27°	6°W
	UVIS	2007-303	2,704,651 km	13°	310°W
	ISS	2006-017	243,916 km	30°	312°W
	VIMS	2006-017	226,162 km	35°	309°W

644

645

646

647

648

649

650

651

Table 2.

Satellite	R_S		E ring grain flux[+] (g/m²/s)	Electron intensity (35 keV)** (electrons cm⁻² s⁻¹ sr⁻¹ keV⁻¹)	Visible albedo*	UV albedo (300 nm)[++]
Mimas	3.08	leading	4.3e-14		0.919	0.583
		trailing	4.3e-12	400.000	1.007	0.639
Enceladus	3.95	leading	3.08e-12		1.328	0.881
		trailing	2.64e-12	260.000	1.424	0.944
Tethys	4.89	leading	1.28e-12		1.287	0.868
		trailing	1.6e-13	1800.00	1.174	0.652
Dione	6.26	leading	9.5e-14		1.233	0.799
		trailing	9.5e-15	4000.00	0.808	0.424
Rhea	8.75	leading	7.2e-16		1.07	0.572
		trailing	8.4e-16	19000.0	0.842	0.439

653   *from Verbiscer et al. (2007)

654   **from Paranicas et al. (2011)

655   [+] estimates to leading and trailing hemispheres from Juhasz and Horanyi (2015)

656   [++]300 nm albedos from Fig. 4

657   R_S – Saturn radii

658

659

660

661

662

663

MIMAS

~230°W, ~43° phase

VIMS
ISS
UVIS

MIMAS

VIMS
ISS
UVIS

664

ENCELADUS

~80°W, ~15° phase

VIMS
ISS
UVIS
HST STIS

ENCELADUS

665

TETHYS LEADING

~60°W, ~10° phase

VIMS
ISS
UVIS
HST STIS

TETHYS LEADING

666

32

TETHYS TRAILING

~250°W, ~60° phase

VIMS
ISS
UVIS
HST STIS

TETHYS TRAILING

667

DIONE LEADING

~110°W, ~26° phase

VIMS
ISS
UVIS
HST FOS

DIONE LEADING

668

DIONE TRAILING

~274°W, ~44° phase

VIMS
ISS
UVIS
HST FOS

DIONE TRAILING

669

670

671
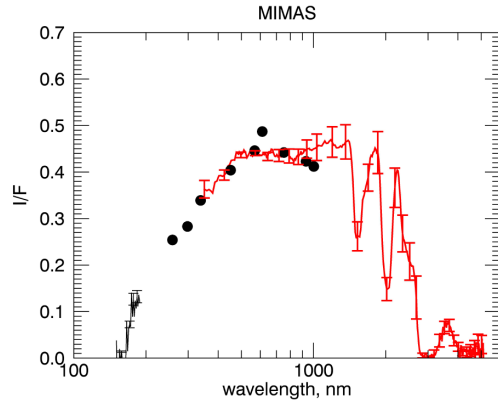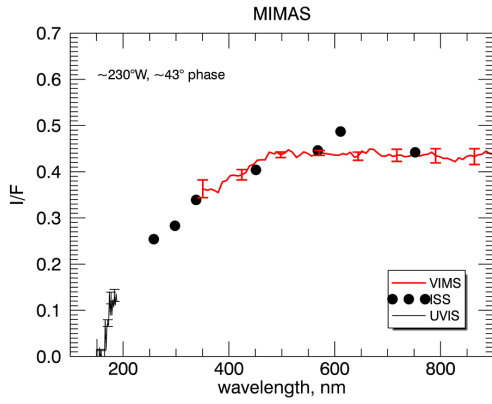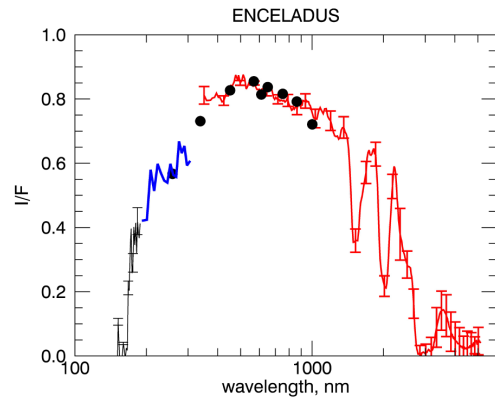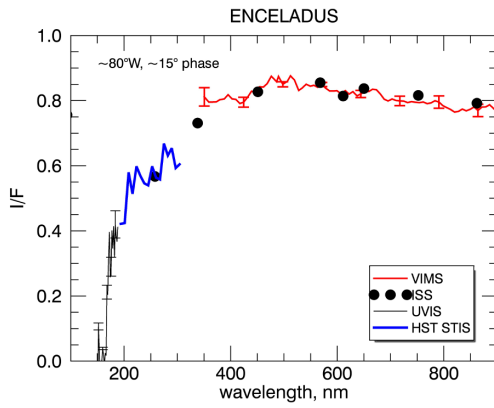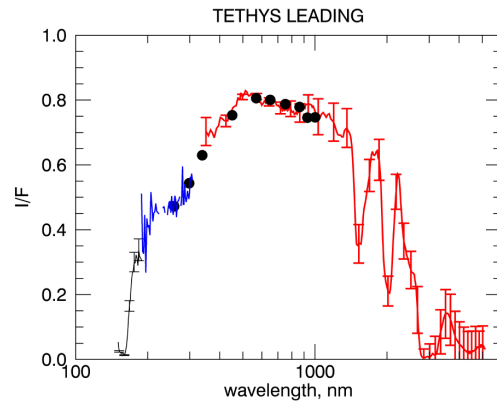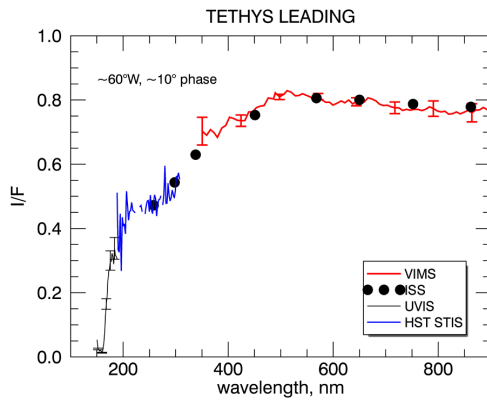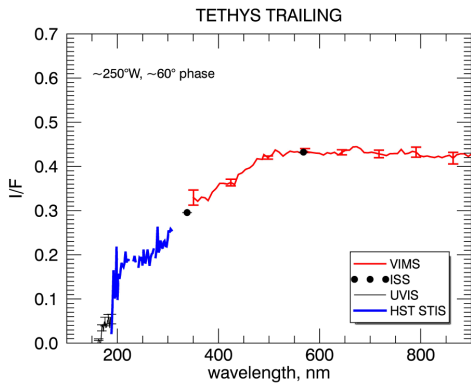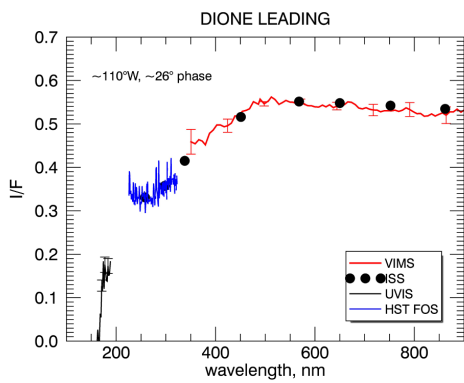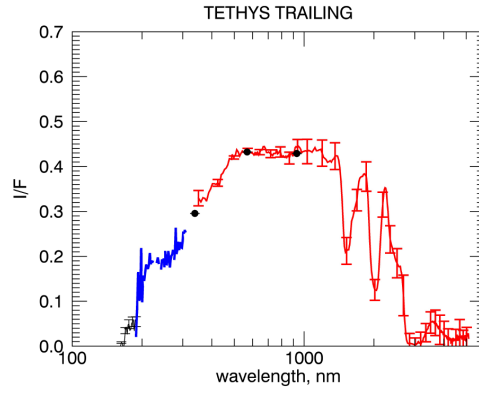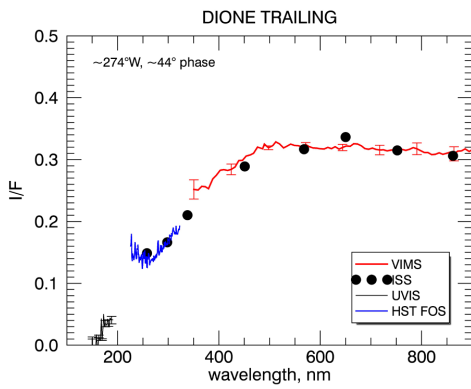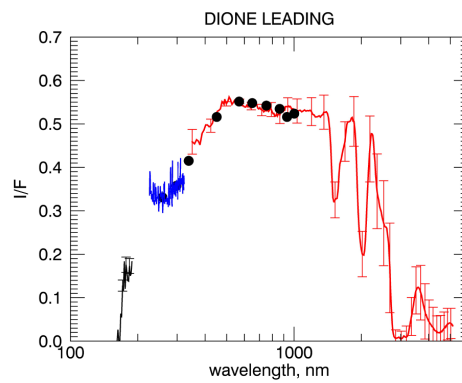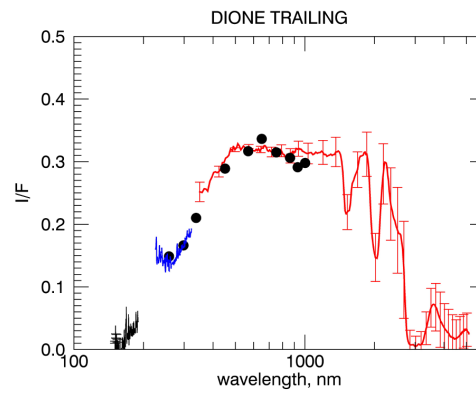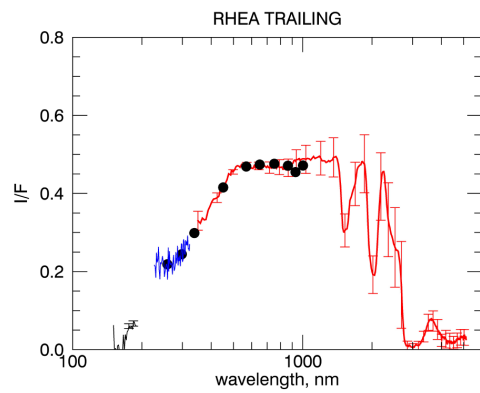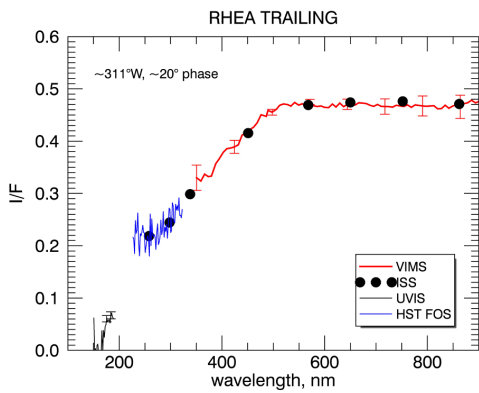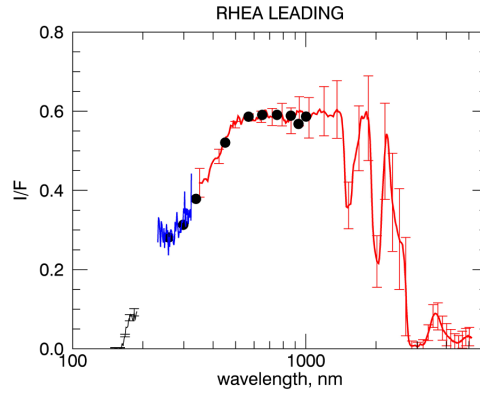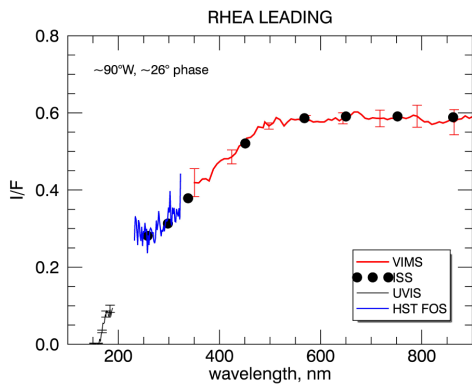
Figure 1. Composite spectra of Mimas, Enceladus, Tethys, Dione and Rhea using data from Cassini UVIS, ISS and VIMS, and HST STIS/FOS. Observational geometry for each observation is indicated in Table 1. Representative error bars for UVIS and VIMS data are shown; the error bars on the ISS data are smaller than the plotting symbol. The HST spectra demonstrate the broad band at 260 nm discussed by Noll et al. (1997).

677

678

679

680

681

682
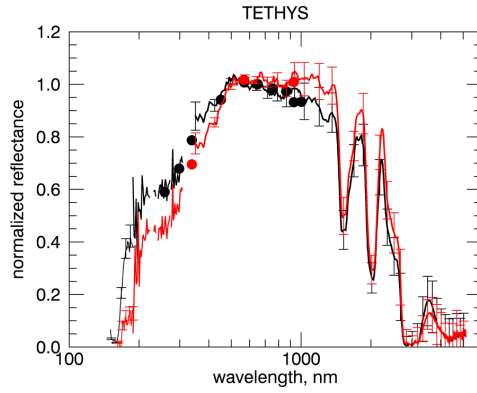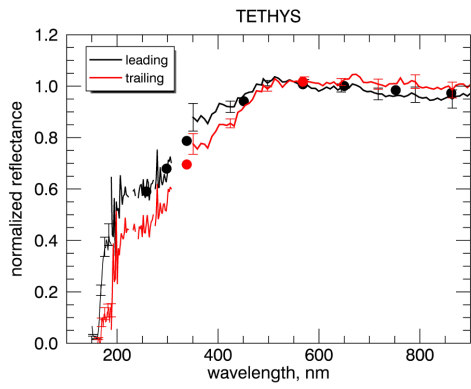
683
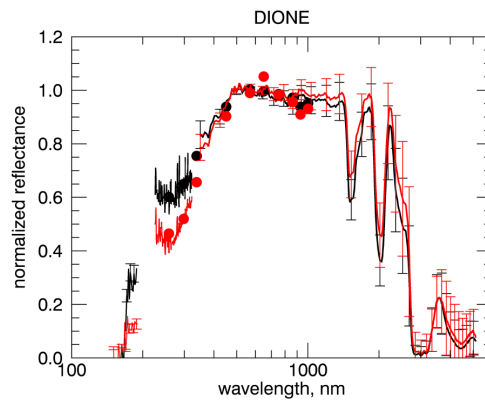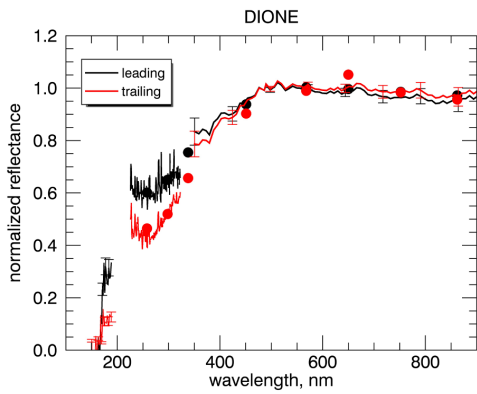
684
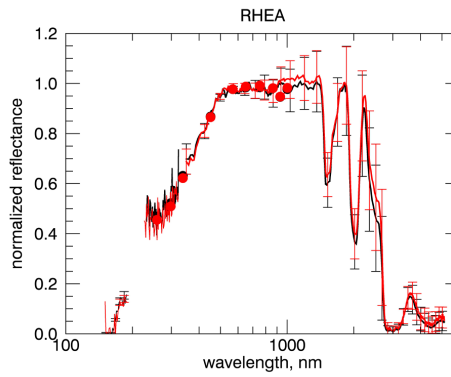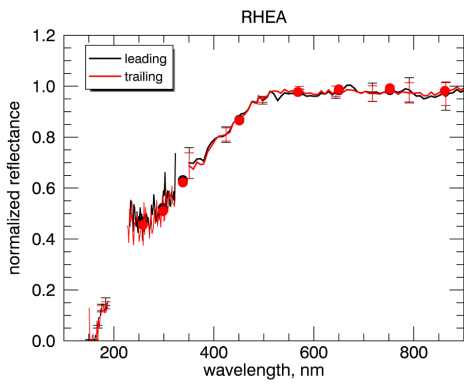
685

686 **Figure 2.** Reflectance spectra, normalized near 600 nm, to directly compare leading and

687 trailing hemispheres of Tethys, Dione and Rhea.

688

689

690

691

692

693
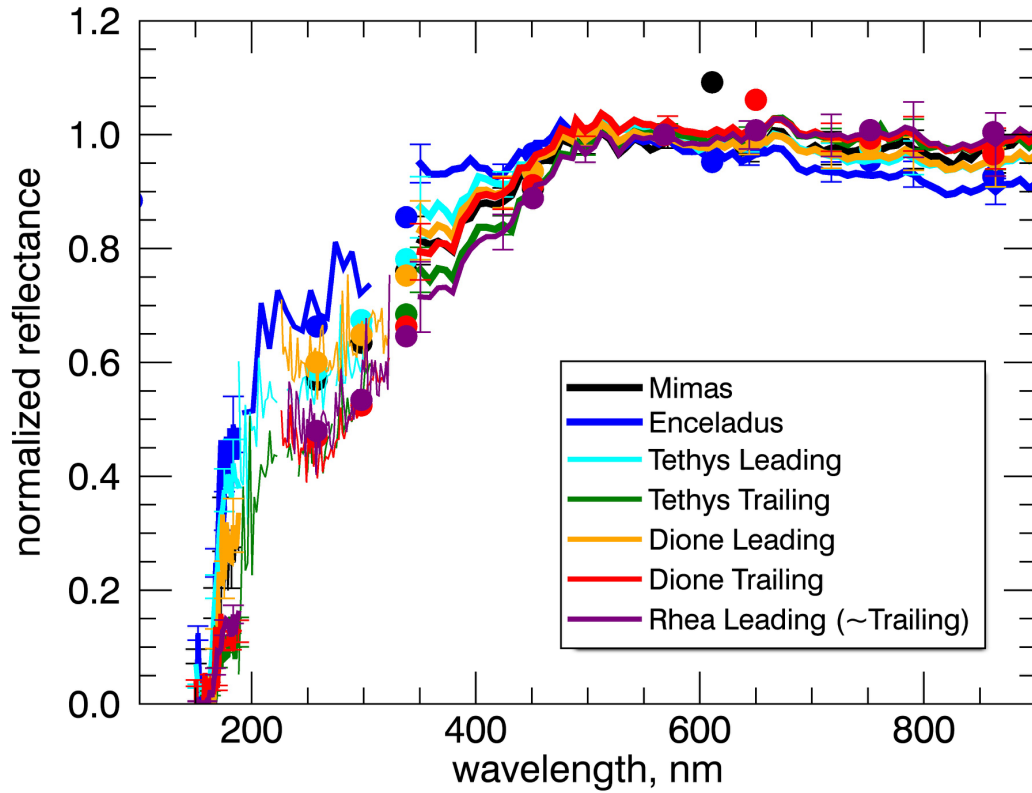
Figure 3. Normalized composite spectra of all satellites using data from UVIS, ISS, HST

and VIMS. The UV absorption edge that begins at ~500 nm is strongest for Rhea, the

trailing hemispheres of Dione and Tethys, and possibly Mimas; it is least strong for

Enceladus and the leading hemispheres of Dione and Tethys. Most of the Mimas data are

hidden by Dione Leading data.

699
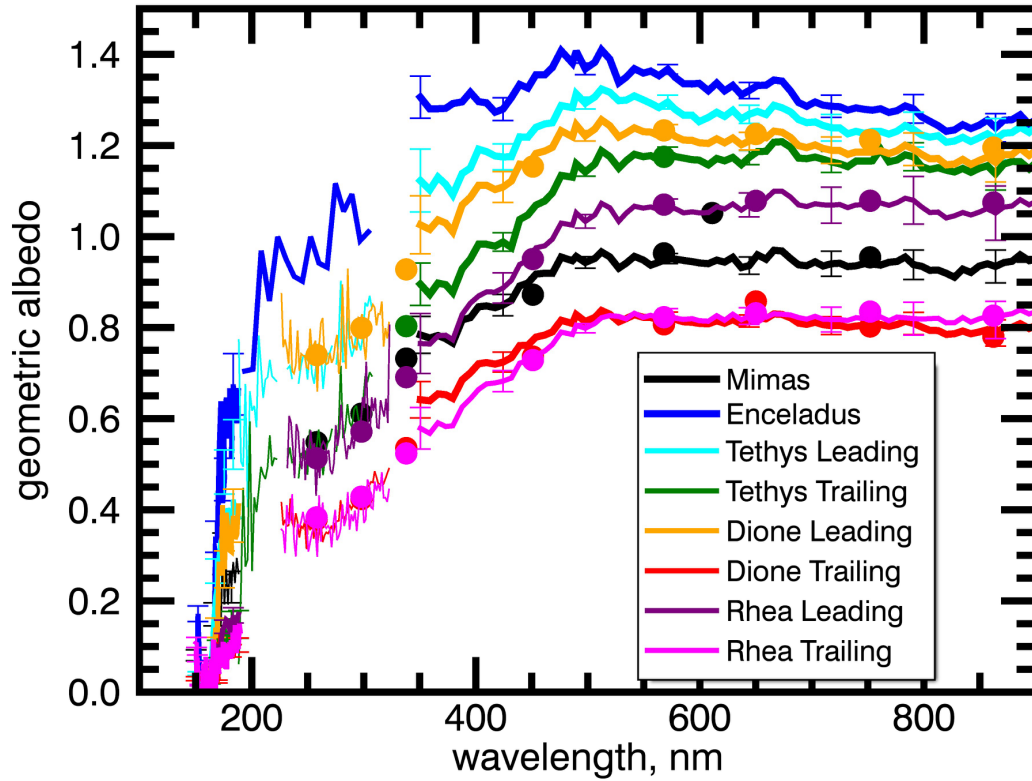
Figure 4. Composite geometric albedo spectra of the Saturnian satellites. To generate these curves, we scale the normalized spectra of Fig. 3 by the visible geometric albedos in Table 2 (from Verbiscer et al., 2007). For Mimas and Enceladus we use average values of 0.963 and 1.376, respectively. Error bars on ISS data are smaller than the plotting symbols.

711

712
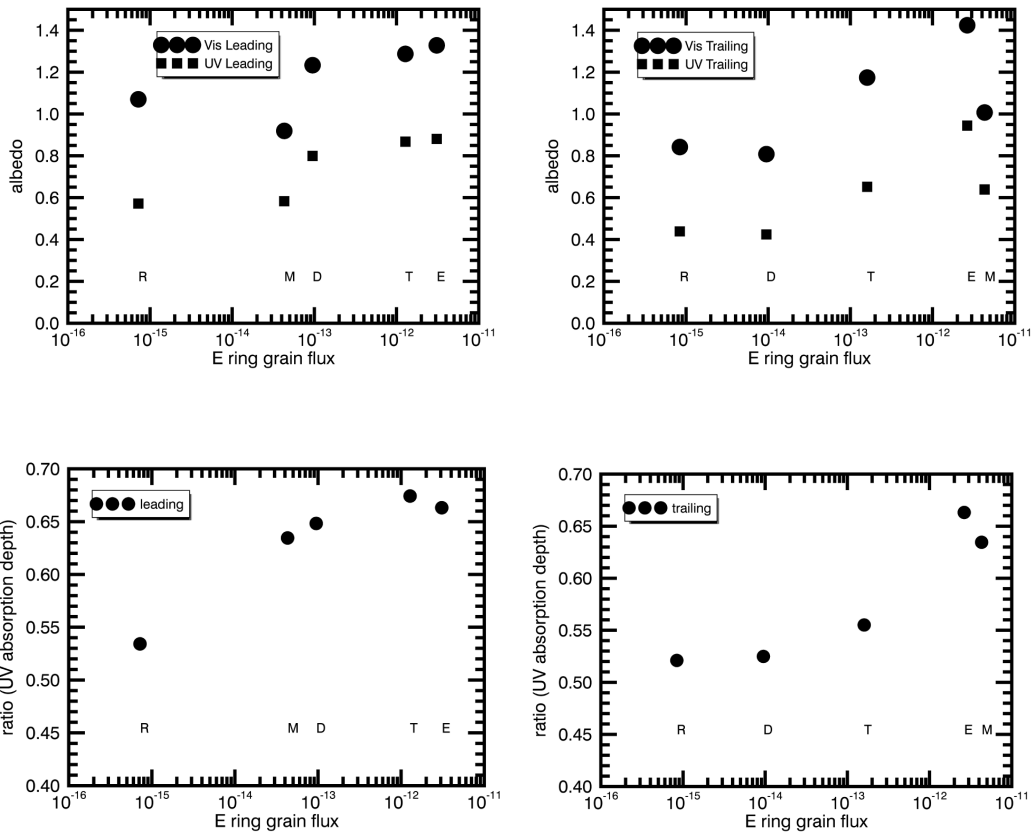
Figure 5. Geometric albedos **(at 300 nm and 600 nm, from Fig. 4)** and UV absorption depth **(where the UV absorption is given by the ratio of the albedo at 300 nm to the albedo at 600 nm)r** are plotted against E ring grain flux on the leading and trailing hemispheres. Horizontal axis units are $g/m^2/s$. On the leading hemisphere (left), there is an association between E ring grain flux and albedo; the correlation is stronger (with lower chi-squared fit values) than on the trailing hemisphere (right). On both leading and trailing hemispheres, there is a relationship between UV absorption and E ring grain flux, with UV absorption increasing with decreasing flux.

721

722

723
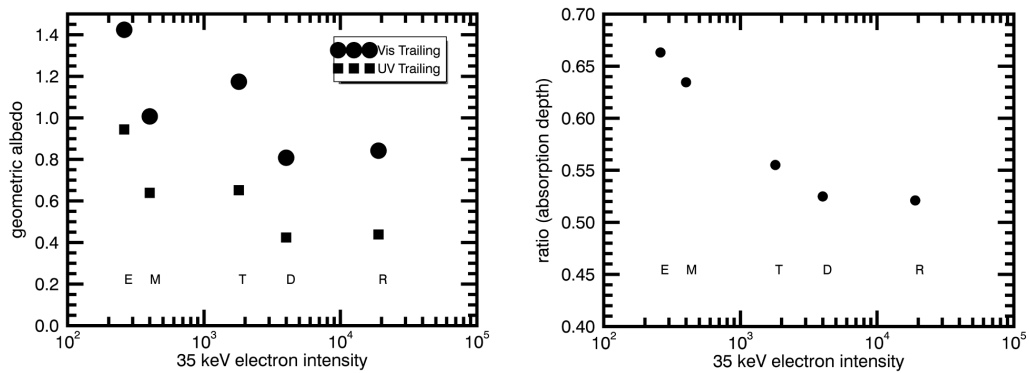
Figure 6. Trailing hemisphere albedo **(at 300 nm and 600 nm, from Fig. 4)** and UV

absorption vs. electron intensity**, where the UV absorption depth is given by the ratio**

of the albedo at 300 nm to the albedo at 600 nm. Horizontal axis units are electrons

cm^{-2} s^{-1} sr^{-1} keV^{-1}. **(top left)** The trailing hemisphere UV and visible albedos roughly

decrease as electron intensity (tens of keV) increases. **(top right)** The UV absorption on

the trailing hemisphere increases with 35 keV electron intensity; the UV absorption is

similar for Tethys, Dione and Rhea, suggesting some level of saturation. These plots use

35 keV electron intensity (Paranicas et al., 2011) as a proxy for ~tens of keV electrons,

which primarily impact the trailing hemispheres.

733

734

735
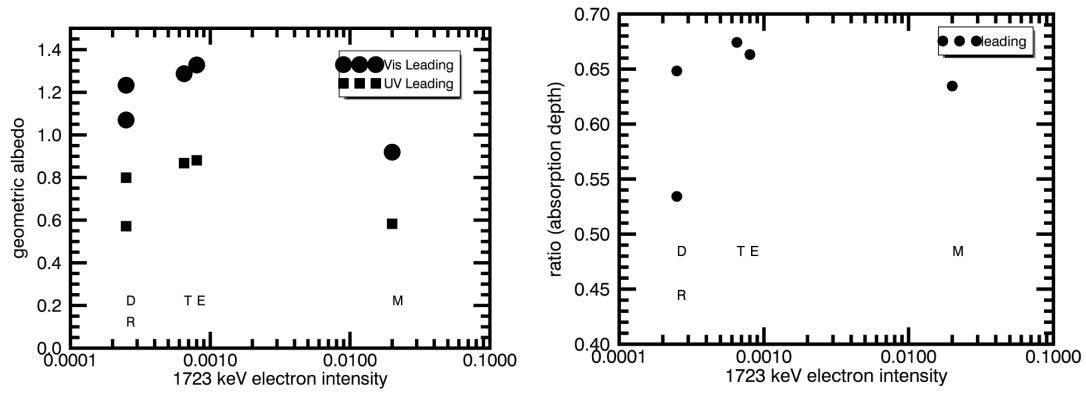
Figure 7. In contrast to the ~tens of keV electrons shown in Fig. 6, ~MeV electrons (Kollmann et al., 2011) (which impact the leading hemispheres) do not demonstrate a coherent relationship with albedo **(left)** or UV absorption depth **(right)**.
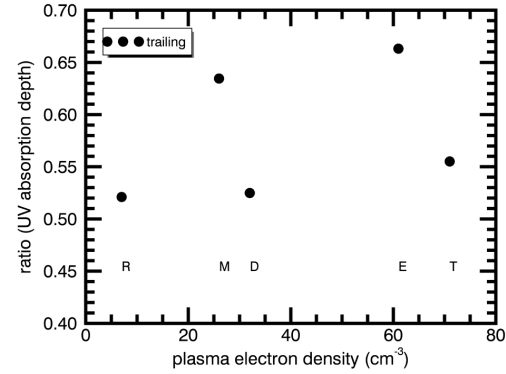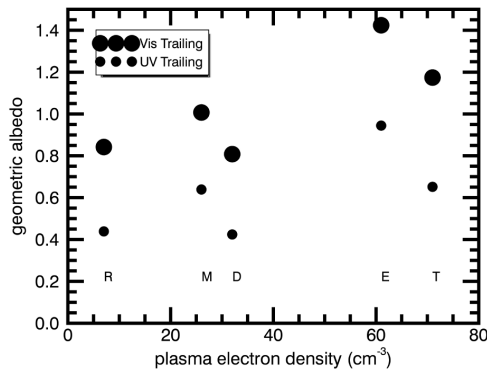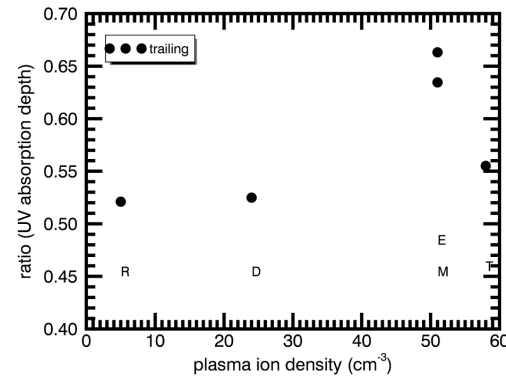
739
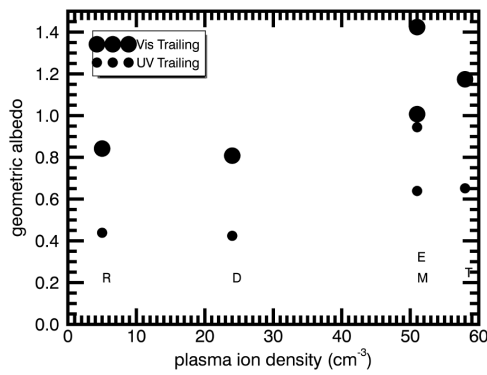
740

741

742

743

744

745

746

747

748

749

750 **Figure 8.** In contrast to the ~tens of keV electrons shown in Fig. 6, cold plasma electrons

751 (Persoon et al., 2006) **(upper)** and cold plasma ions (Persoon et al., 2009) **(lower)** (both

752 of which impact the trailing hemispheres) do not demonstrate a coherent relationship with

753 albedo **(left)** or UV absorption depth **(right)**.

754

755